High-Li^+-fraction ether-side-chain pyrrolidinium–asymmetric imide ionic liquid electrolyte for high-energy-density Si//Ni-rich layered oxide Li-ion batteries

Bharath Umesh [a], Purna Chandra Rath [b], Jagabandhu Patra [b,c], Rahmandhika Firdauzha Hary Hernandha [b], Subhasis Basu Majumder [d], Xinpei Gao [e], Dominic Bresser [e,f], Stefano Passerini [e,f], Hong-Zheng Lai [g], Tseng-Lung Chang [g], Jeng-Kuei Chang [a,b,c,*]

[a] *Institute of Materials Science and Engineering, National Central University, 300 Jhong-Da Road, Taoyuan 32001, Taiwan*
[b] *Department of Materials Science and Engineering, National Yang Ming Chiao Tung University, 1001 University Road, Hsinchu 30010, Taiwan*
[c] *Hierarchical Green-Energy Materials (Hi-GEM) Research Center, National Cheng Kung University, 1 University Road, Tainan 70101, Taiwan*
[d] *Materials Science Centre, Indian Institute of Technology, Kharagpur 721302, West Bengal, India*
[e] *Helmholtz Institute Ulm (HIU), 89081 Ulm, Germany*
[f] *Karlsruhe Institute of Technology (KIT), 76021 Karlsruhe, Germany*
[g] *SolidEdge Solution Inc., Taiwan*

ARTICLE INFO

Keywords:
Si composite anode
Electrolyte design
High safety
Li^+ concentration
Al corrosion
Rate capability

ABSTRACT

In this study, Si nanoparticles with interweaving carbon nanotubes are wrapped by graphitic sheets to achieve high conductivity and high dimensional stability of a composite anode (denoted as Si/CNT/G) for Li-ion batteries. In addition, an ionic liquid (IL) electrolyte that consists of ether-side-chain pyrrolidinium, asymmetric imide, and a high Li^+ fraction is prepared. This electrolyte is for the first time employed for Si-based Li-ion batteries. Decomposition of the ether groups creates organic components in the solid electrolyte interphase (SEI). The high Li^+ concentration promotes decomposition of the (fluorosulfonyl)(trifluoromethanesulfonyl)imide (FTFSI) anions, leading to a LiF- and Li_3N-rich SEI. The organic-inorganic balanced SEI is responsible for the excellent charge-discharge properties of the Si/CNT/G anode. The FTFSI anions exhibit low corrosivity toward the Al current collector and high compatibility with the $LiNi_{0.8}Co_{0.1}Mn_{0.1}O_2$ (NCM-811) cathode. With a charging voltage of 4.5 V, remarkable reversible capacities and cycling stability of NCM-811 in the high-Li^+-fraction *N*-methoxyethyl-*N*-methylpyrrolidinium/FTFSI IL electrolyte are observed. Differential scanning calorimetry is used to examine the interfacial exothermic reactions between the delithiated NCM-811 and various electrolytes. After 300 charge-discharge cycles, the capacity retention of a Si/CNT/G||NCM-811 full cell with the proposed IL electrolyte is 80% with a Coulombic efficiency of ~99.9%. These values are significantly higher than those of the conventional carbonate electrolyte cell.

1. Introduction

Portable electronic devices and electric vehicles require efficient high-performance energy storage and a decarbonized economy requires grid-scale energy stabilization. Lithium-ion batteries (LIBs) can play a crucial role in these applications. However, despite decades of progress, the energy and power densities of present LIBs remain unsatisfactory and cannot completely meet the increasing application requirements [1,2]. Thus, the development of anodes with high capacities and cathodes with high operation potential and high capacities has become an important field of research [3–5]. The conventional carbonaceous anodes used in LIBs (e.g., graphite) have limited capacities (i.e., ~350 mAh g^{-1}) [6]. Anodes based on Si, which has a high theoretical capacity (i.e., 3579 mAh g^{-1}, assuming the formation of $Li_{15}Si_4$), high abundance, and low toxicity, have attracted a lot of attention [7,8]. Nevertheless, the implementation of Si anodes is challenging because the severe volume

* Corresponding author at: 1001 University Road, National Yang Ming Chiao Tung University, Hsinchu, Taiwan.
E-mail address: jkchang@nctu.edu.tw (J.-K. Chang).

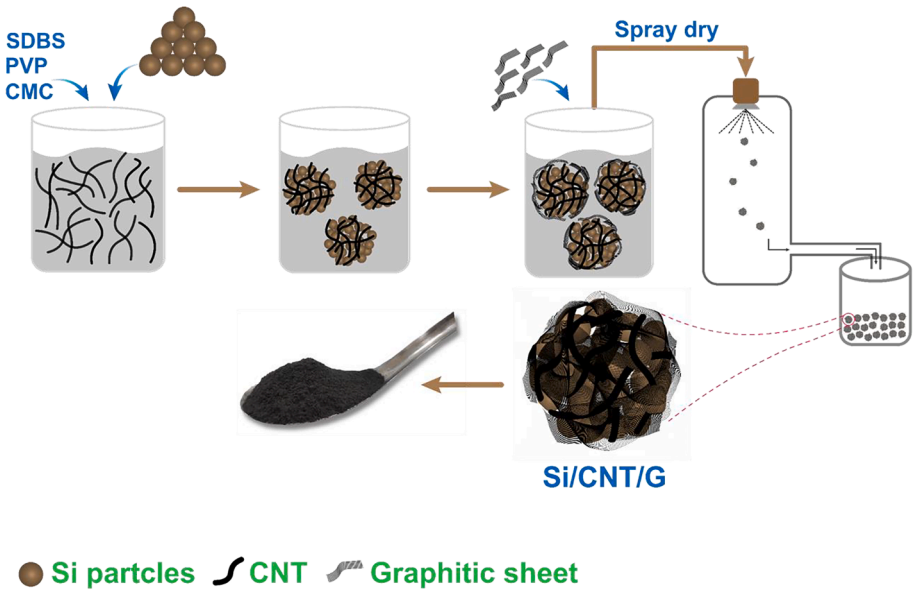

Fig. 1. Scheme of synthesis of Si/CNT/G composite.

change of ~400% during lithiation/delithiation leads to an unstable electrode/electrolyte interface and thus fast capacity degradation [9]. Several strategies, including Si size and morphology control [10], nano-architecture design [11–13], composite structure construction [14], and binder optimization [15], have been adopted to enhance Si anode cyclability. Some studies have been conducted on the electrolyte, which can increase the cycling stability of Si electrodes [16,17]. However, the ideal electrolyte for Si-based anodes is not yet clear. An appropriate electrolyte that can form a reliable solid electrolyte interphase (SEI) on Si-based electrodes is required.

Room-temperature ionic liquids (ILs) are a promising type of LIB electrolyte owing to their wide electrochemical stability windows, high thermal stability, non-volatility, and environmental friendliness [18–21]. ILs have also been employed to synthesize high-conductivity fluoride solid electrolytes [22,23]. Bis(fluorosulfonyl)imide (FSI^-)-based ILs were found to be highly suitable for Si anodes [24,25]. Such ILs can form a robust SEI, which results in high Si capacities and long cycle life [26]. However, the FSI^- anion is not able to prevent the Al current collector dissolution at above ~4 V vs. Li/Li^+ [27,28]. This has restricted the practical utilization of FSI^--based ILs for high-voltage LIBs. Another main constraint of FSI^--based ILs is the formation of solid, crystalline complexes at low temperature [29]. It has been found that the introduction of asymmetric (fluorosulfonyl)(trifluoromethanesulfonyl)imide ($FTFSI^-$) anions inhibits the crystallization of ILs and reduces their freezing points [30]. Nevertheless, the corrosivity of $FTFSI^-$ toward Al needs to be further examined. Moreover, the electrochemical behavior of Si anodes in $FTFSI^-$-based ILs has not been examined. These two issues are considered in the present study. Regarding IL cations, conventional pyrrolidinium ions with alkyl side chains tend to form ion aggregates, which increase electrolyte viscosity and thus decrease ion mobility [31]. The introduction of a flexible ether functionality in the pyrrolidinium side chain (as, e.g., in *N*-methoxyethyl-*N*-methylpyrrolidinium (Pyr_{12O1}^+)) can reduce self-aggregation and improve IL fluidity as well as ionic conductivity [32]. Moreover, the presence of the ether group decreases the glass transition temperature, thus extending the operation temperature range of the electrolyte. For IL electrolytes, the unsatisfactory rate capability of electrodes at room temperature has long been a challenge [33]. The combination of Pyr_{12O1}^+ and $FTFSI^-$ has great potential to form an IL electrolyte that can overcome this obstacle because of its high fluidity and low crystallization temperature. The use of Pyr_{12O1}FTFSI-based IL electrolyte for Si anodes is for the first time investigated herein.

To achieve high energy density for LIBs, high-voltage cathodes with high capacities are required. Unfortunately, in the development of electrolytes for Si anodes, the electrolyte compatibility at the cathode side is usually overlooked. The side reactions at high potential, such as electrolyte decomposition and interface deterioration, are major concerns [34]. In addition, the attack by the electrolyte on the Al current collector needs to be minimized. In fact, the required properties of electrolytes for the cathode side are different from those for the anode side. However, few studies have aimed to develop a balanced electrolyte taking into consideration both the Si anode and high-voltage cathode performance. This topic is hence addressed in the present work.

In this study, a Si/carbon nanotube/graphitic sheet (Si/CNT/G) composite anode is developed and examined in the Pyr_{12O1}FTFSI IL electrolyte, which forms liquid mixtures with LiFTFSI in a wide molar ratio range. The roles of the LiFTFSI fraction in the SEI chemistry, as well as the Si anode performance, are investigated. The proposed IL electrolyte with a LiFTFSI/Pyr_{12O1}FTFSI molar ratio of 4:6 enables excellent rate capability and cyclability of the Si/CNT/G anode, clearly outperforming Pyr_{13}FSI (Pyr_{13} *N*-propyl-*N*-methylpyrrolidinium), Pyr_{13}TFSI (TFSI bis(trifluoromethanesulfonyl)imide), and conventional 1 M $LiPF_6$ carbonate electrolytes in terms of electrode performance. Furthermore, the proposed IL electrolyte shows great compatibility with a Ni-rich $LiNi_{0.8}Co_{0.1}Mn_{0.1}O_2$ (NCM-811) cathode, which exhibits a high specific capacity of >200 mAh g^{-1} at high charging voltage of 4.5 V (vs. Li^+/Li). To examine safety, the exothermic interactions between the delithiated NCM-811 electrodes and various electrolytes are examined using differential scanning calorimetry (DSC). In addition, Si/CNT/G||NCM-811 full cells with various electrolytes are constructed, and their charge–discharge properties are investigated. The proposed high-LiFTFSI-fraction Pyr_{12O1}FTFSI-based IL electrolyte is promising for high-safety and high-energy–density Si-based LIBs.

2. Experimental section

2.1. Electrode materials and electrolytes

Si/CNT/G composite powder was fabricated via a spray-drying method. First, CNTs (LG Chem; purity: >97%; diameter: 8–12 nm; length: 5–8 μm; Brunauer-Emmett-Teller (BET) surface area: 220 m^2 g^{-1}) were dispersed in a solution of sodium dodecylbenzenesulfonate (SDBS), polyvinylpyrrolidone (PVP), carboxymethyl cellulose (CMC), ethanol, and deionized water, producing a homogeneous CNT

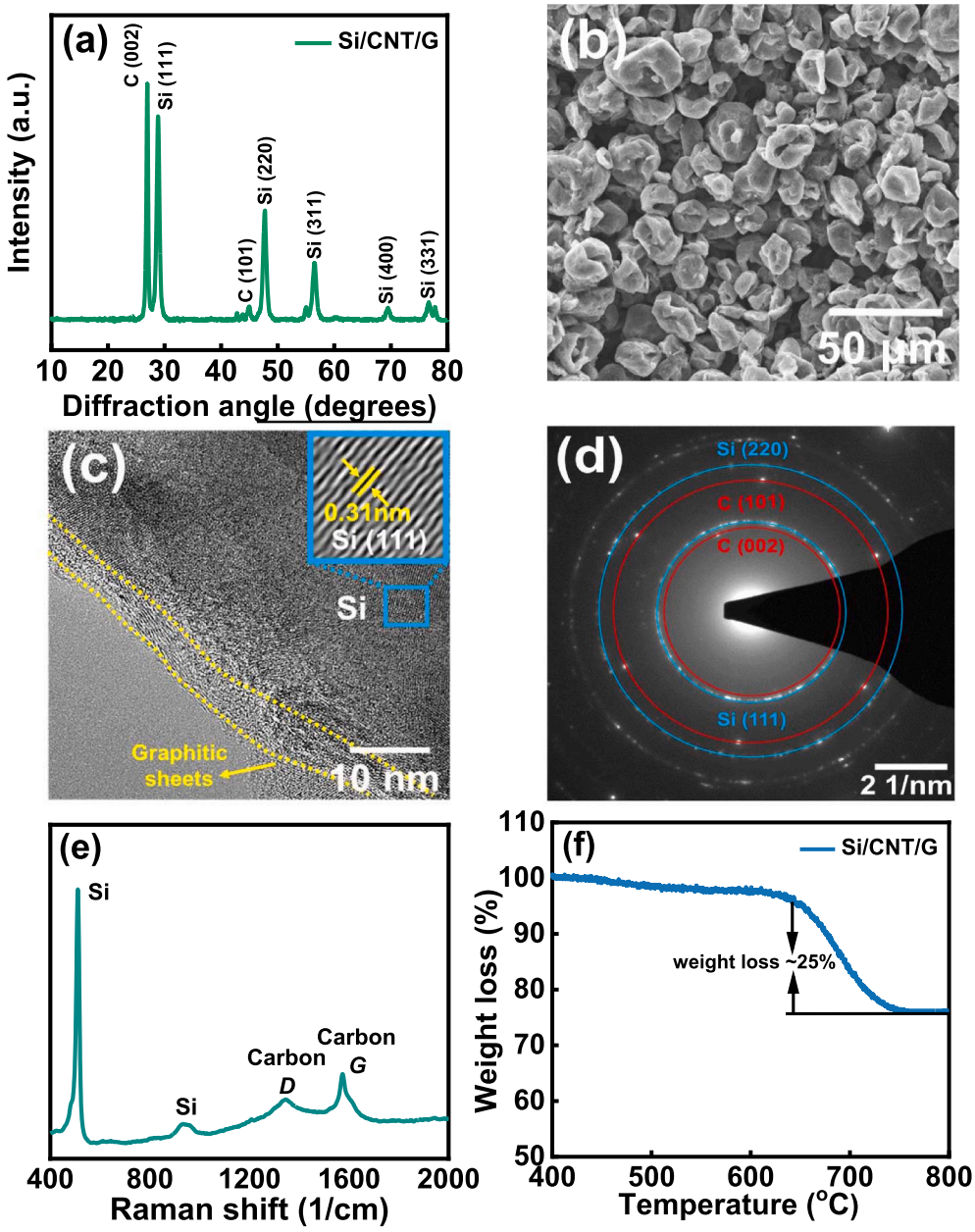

Fig. 2. (a) XRD pattern, (b) SEM image, (c) high-resolution TEM image, (d) electron diffraction pattern, (e) Raman spectra, and (f) TGA data of Si/CNT/G sample.

suspension. Si powder (Super Energy Material Inc., Taiwan; purity: >99.5%; D_{50}: ~100 nm) was then added into the above suspension, which was stirred for 1 h. Afterward, graphitic sheets (Taiwan Carbon Materials Corp.; purity: >99.5%; BET surface area: 10–15 $m^2\ g^{-1}$) were introduced (with a graphitic sheet to CNT weight ratio of 50:1) and mixed by wet milling. The resulting solution was spray-dried to obtain a Si/CNT/G powdery sample. NCM-811 powder was purchased from Ubiq Technology Co. Ltd. $Pyr_{12O1}FTFSI$ IL was synthesized using procedures reported in a previous paper [35]. $Pyr_{13}FSI$ and $Pyr_{13}TFSI$ ILs (purity: 99.9%) were purchased from Solvionic and vacuum-dried at 80 °C for 24 h before use. Battery-grade LiFSI and LiTFSI were purchased from Kishida Chemical. All the electrolytes were prepared in an argon-filled glove box and dried over fresh molecular sieves before use. The water content of the electrolytes, measured using Karl Fisher titration, was below 20 ppm.

2.2. Cell assembly

The negative electrode slurry was prepared by mixing 88 wt% Si/CNT/G powder, 1 wt% carbon black, and 11 wt% sodium polyacrylate binder in deionized water. The obtained slurry was cast onto Cu foil using a doctor blade and then vacuum-dried at 100 °C for 10 h. The Si/CNT/G mass loading was ~2.5 mg cm^{-2}. The positive electrode slurry was prepared by mixing 80 wt% NCM-811, 10 wt% Super P, and 10 wt% polyvinylidene fluoride binder in *N*–methyl-2-pyrrolidone. The obtained slurry was cast onto Al foil and then vacuum-dried at 110 °C for 10 h. The NCM-811 mass loading was ~5 mg cm^{-2}. The electrodes were punched to match the required dimensions of a CR 2032 cell. Li foil and a glass fiber membrane were used as the counter electrode and separator, respectively. The assembly of the coin cells was conducted in an argon-filled glove box (Vigor Tech. Co. Ltd.), where both the moisture content and oxygen content were maintained at below 0.1 ppm.

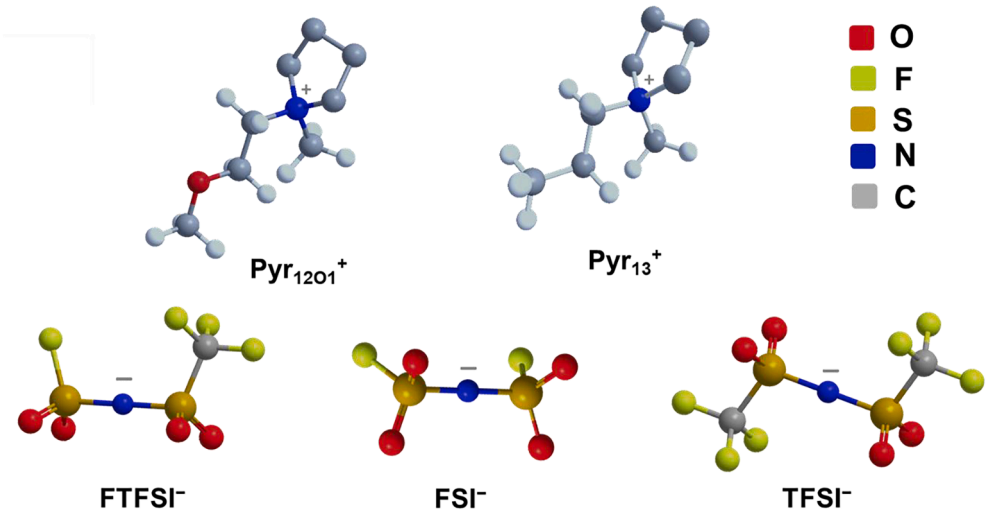

Fig. 3. Molecular structures of the IL cations and anions used in this study.

2.3. Material and electrochemical characterizations

The crystallinity of Si/CNT/G was characterized using X-ray diffraction (XRD; Bruker D2 PHASER). The morphologies and microstructures of the samples were examined using scanning electron microscopy (SEM; FEI Inspect F50) and transmission electron microscopy (TEM; JEOL 2100F). Raman data were collected using a LabRAM HR 800 spectrometer (with a laser wavelength of 633 nm). TGA (Perkin-Elmer TGA7) was conducted under air with a heating rate of 5 °C min^{-1}. X-ray photoelectron spectroscopy (XPS; Thermo Fisher Scientific ESCALAB Xi^+) was employed to examine the surface chemical composition of various electrodes. Al Kα radiation (1486.6 eV) was used as the X-ray source. The data fitting was conducted using the XPSPEAK 4.1 software. The charge–discharge properties (such as capacity, rate capability, and cycling stability) of various cells were evaluated using an Arbin BT-2043 battery tester at 25 °C. The voltage ranges used for the Si/CNT/G and NCM-811 half cells were 0.05–2.0 V and 2.7–4.5 V, respectively. To construct Si/CNT/G||NCM-811 full cells with various electrolytes, an anode-to-cathode capacity ratio of ~1.2 was used. The Si/CNT/G anode was pre-conditioned for three cycles and prelithiated by 20% in a half cell prior to the full cell assembly. For each testing condition, at least 5 duplicate cells were measured. The performance deviation was typically within 5%. The reported data are the median values. Electrochemical impedance spectroscopy (EIS) measurements were carried out with a Biologic VSP-300 potentiostat in a frequency range of 10^6–10^{-2} Hz with an AC amplitude of 10 mV. The thermal stability of the NCM-811 samples delithiated in various electrolytes was evaluated using DSC (Netzsch DSC3500) in a temperature range of 50–350 °C. The NCM-811 powder was recovered from the coin cells after delithiation to 4.5 V and then placed into Al capsules in the glove box without washing and drying. The samples were heated at a rate of 10 °C min^{-1} under an N_2 atmosphere in the DSC chamber.

3. Results and discussion

Si/CNT/G composite powder was fabricated via a spray-drying method. Fig. 1 shows the scheme of the synthesis. With the SDBS surfactant, the CNTs and Si particles were well dispersed in the solution. The Si particles with interweaving CNTs were then surrounded by the graphitic sheets introduced later. After the spray drying, the Si/CNT clusters were wrapped by the graphitic sheets via the PVP/CMC binder. The crystal structure of the Si/CNT/G was examined using XRD; the obtained pattern is shown in Fig. 2(a). The diffraction peaks located at 28.5°, 47.5°, 56.1°, 69.5°, and 76.7° are associated with the (111), (220), (311), (400), and (331) planes of polycrystalline Si, respectively. Graphitic carbon (002) and (101) diffractions appear at 26.2° and 45°, respectively. Fig. 2(b) shows an SEM image of the Si/CNT/G particles, which have a ball-like morphology with a diameter of approximately 10 μm after spray drying. The high-resolution TEM image in Fig. 2(c) shows that the Si nanoparticles were well mixed and integrated with CNTs and graphitic sheets. Fig. 2(d) shows the corresponding electron diffraction pattern, in which the Si and graphitic carbon diffraction signals can be clearly observed. The Raman spectrum of the Si/CNT/G sample is shown in Fig. 2(e). The peaks at ~520 and ~960 cm^{-1} are ascribed to the vibration bands of polycrystalline Si [36]. The signals at ~1345 cm^{-1} and ~1595 cm^{-1} correspond to the carbon *D* and *G* bands, respectively. The former is related to imperfect carbon bonding and the latter results from the Raman-allowed in-plane vibration of sp^2 carbon [37]. The carbon content in the Si/CNT/G composite was examined by thermogravimetric analysis (TGA). The data in Fig. 2(f) show a clear weight loss at around 625–750 °C due to the burnout of carbon species. It is noted that the Si oxidation mainly happens above 800 °C, which is outside the temperature range of our TGA measurement. The results indicate that the carbon content of the Si/CNT/G sample is around 25 wt%.

LiFTFSI was mixed with Pyr_{12O1}FTFSI in molar ratios of 2:8 and 4:6 (denoted as Pyr_{12O1}FTFSI-1 and Pyr_{12O1}FTFSI-2, respectively). The electrolyte with LiFSI and Pyr_{13}FSI with a molar ratio of 2:8 is denoted as IL-3, and that with LiTFSI and Pyr_{13}TFSI with a molar ratio of 1:9 is denoted as IL-4. Note that LiTFSI/Pyr_{13}TFSI liquid mixtures occur in a narrow molar ratio range, and thus a higher Li^+ fraction cannot be achieved without precipitation of a crystalline complex. The molecular structures of the IL cations and anions are shown in Fig. 3. The viscosity, ionic conductivity, Li^+ transference number, and glass transition temperature of the ILs are shown in Table S1. To examine the compatibility of the Si/CNT/G electrode with various IL electrolytes, galvanostatic tests were performed. Fig. S1(a) (d) show the initial three charge–discharge curves measured at 50 mA g^{-1}. The cells with Pyr_{12O1}FTFSI-1, Pyr_{12O1}FTFSI-2, IL-3, and IL-4 electrolytes showed initial Coulombic efficiency (CE) values of 78%, 80%, 76%, and 36%, respectively. The efficiency loss can be mainly ascribed to the reductive decomposition of the electrolyte, which led to the formation of the SEI [38]. The relatively high CE values found for Pyr_{12O1}FTFSI-based ILs are associated with a superior SEI that better stabilized the electrode surface (the details are examined later). The results suggest that the $TFSI^-$-derived SEI passivated the Si/CNT/G electrode, hindering subsequent lithiation/delithiation reactions. For comparison, the initial CE value of the same electrode in the conventional electrolyte, consisting of 1 M

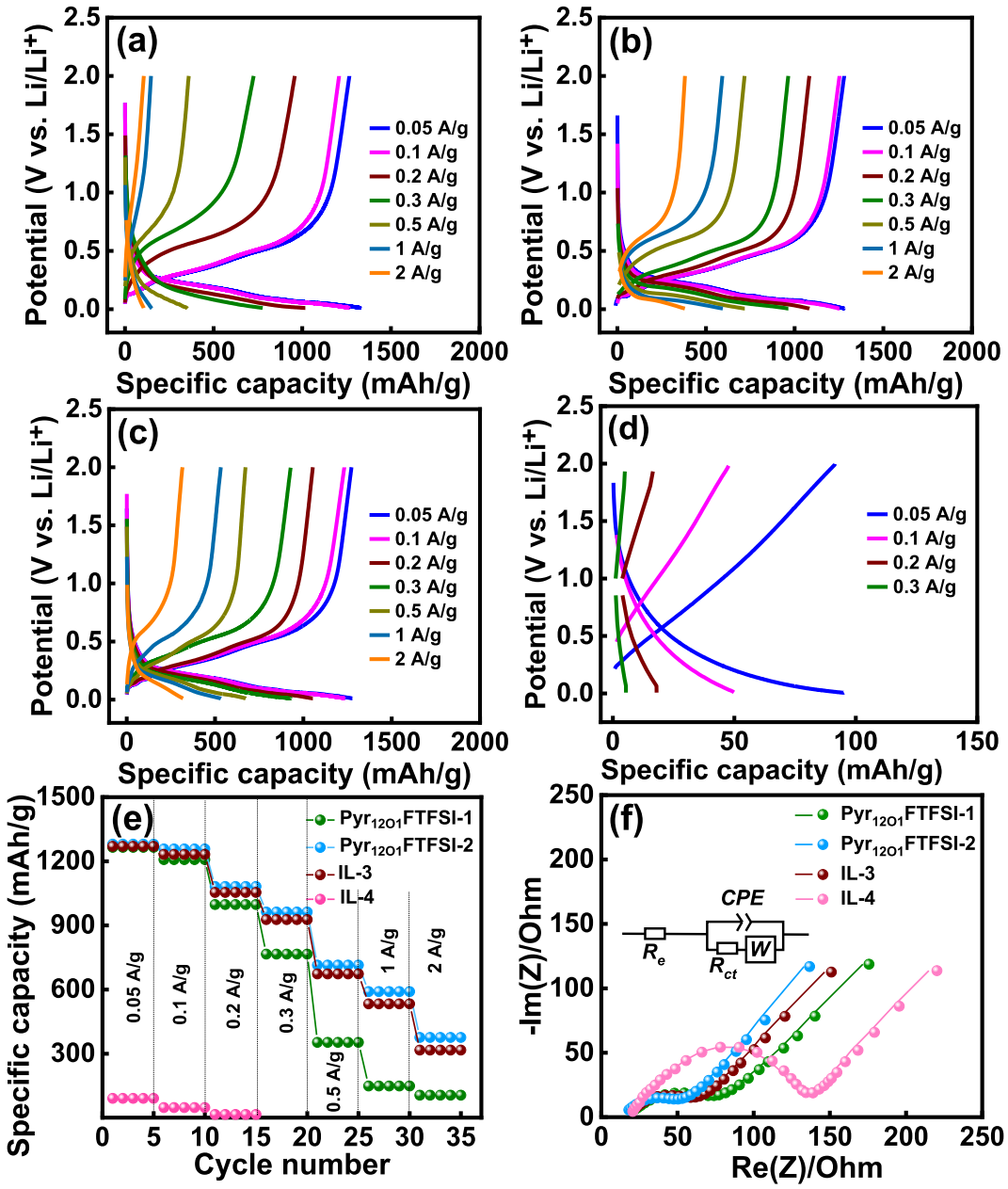

Fig. 4. Charge-discharge curves of Si/CNT/G electrodes recorded in (a) Pyr_{1201}FTFSI-1, (b) Pyr_{1201}FTFSI-2, (c) IL-3, and (d) IL-4 electrolytes at various current rates. (e) Comparative rate performance of various cells. (f) EIS spectra of various cells and equivalent circuit used for data fitting (solid spheres represent data points and solid lines represent fitting curves).

Table 1
Reversible capacities (mAh g ^{1}) of Si/CNT/G electrodes measured at various rates in IL electrolytes.

Specific current (A/g)	Pyr_{1201}FTFSI-1	Pyr_{1201}FTFSI-2	IL-3	IL-4
0.05	1265	1280	1270	92
0.1	1207	1253	1231	47
0.2	998	1082	1054	16
0.3	776	963	927	4
0.5	352	718	673	<1
1	149	593	533	<1
2	106	384	317	<1
$\frac{\text{Capacity@2 A/g}}{\text{Capacity@0.05 A/g}}$(%)	8	30	25	<1

$LiPF_6$ in ethylene carbonate (EC)/diethyl carbonate (DEC) (1:1 by volume) mixed solvent, was 75% (Fig. S2). A high initial CE is important for Si-based anodes with regard to their potential practical applicability.

Fig. 4(a) (d) show the charge–discharge profiles (after two conditioning cycles) of the Si/CNT/G electrodes measured at various specific currents with different electrolytes. At 50 mA g^{-1}, reversible capacities of 1265, 1280, 1270, and 92 mAh g^{-1} were found for the Pyr_{1201}FTFSI-1, Pyr_{1201}FTFSI-2, IL-3, and IL-4 electrolytes, respectively. With increasing charge–discharge rate, the specific capacities decreased, as shown in Fig. 4(e). Table 1 reveals that the specific capacities measured in the electrolytes decreased to 106, 384, 317, and <1 mAh g^{-1}, respectively, at a specific current of 2 A g^{-1}, corresponding to 8%, 30%, 25%, and <1% of the capacities found at 0.2 A g^{-1}. The higher Li^+ fraction of Pyr_{1201}FTFSI-2 (compared to that of Pyr_{1201}FTFSI-1) allows greater Li^+ availability and a higher Li^+ transference number [39], leading to a superior rate capability. The rate capability is even better

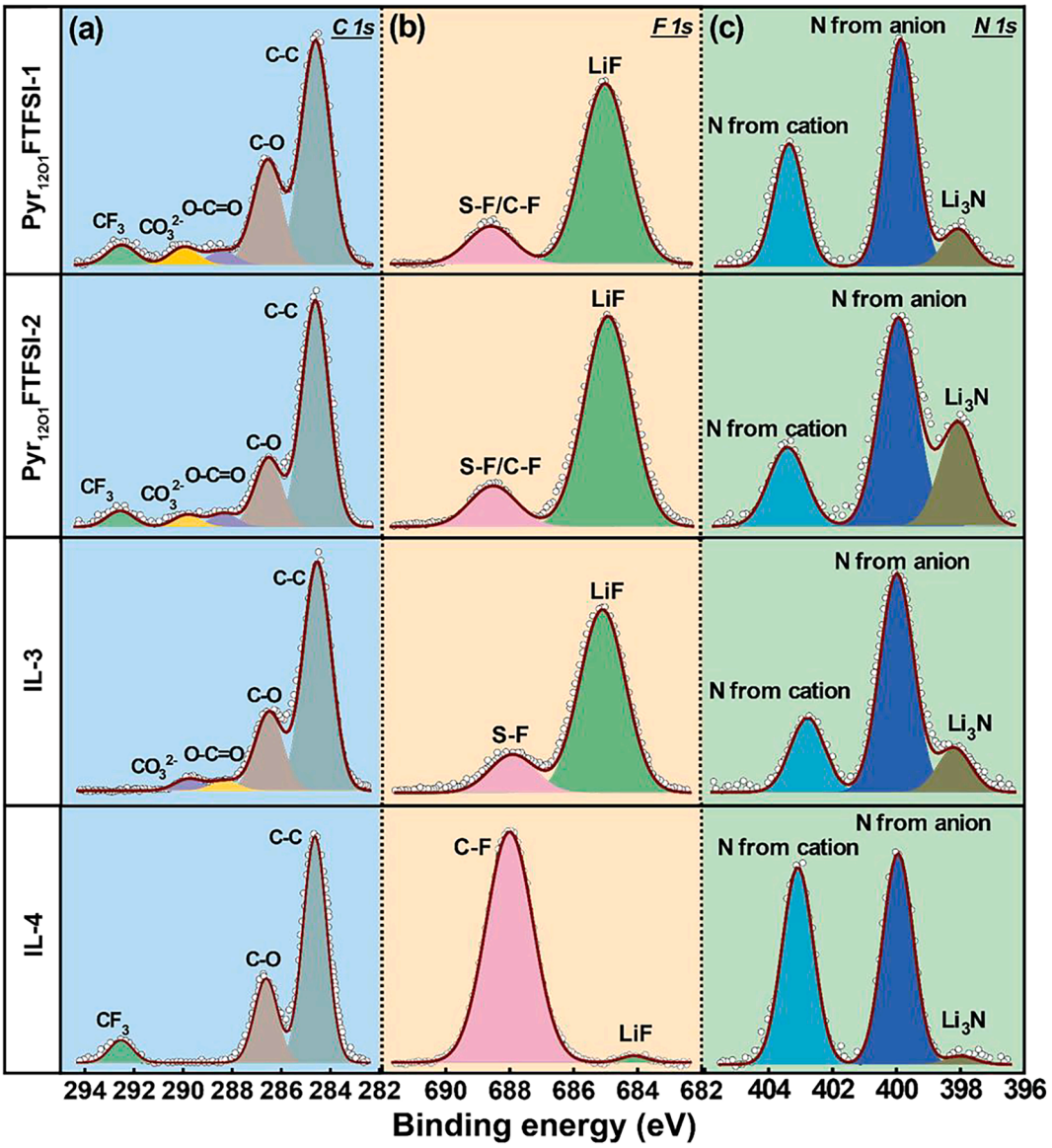

Fig. 5. XPS (a) C 1s, (b) F 1s, and (c) N 1s spectra of Si/CNT/G electrodes after being cycled for three times in Pyr_{12O1}FTFSI-1, Pyr_{12O1}FTFSI-2, IL-3, and IL-4 electrolytes.

than that of IL-3, which is known to enable excellent high-rate performance of Si anodes [26]. We tried to increase the LiFSI molar ratio in the Pyr_{13}FSI IL and found that the maximal ratio is approximately 3:7 (due to the solubility limit). As shown in Fig. S3, the high-rate specific capacities found for the LiFSI/Pyr_{13}FSI 3/7 electrolyte only marginally increase compared to those for IL-3 (i.e., are still clearly lower than those of Pyr_{12O1}FTFSI-2). The cell with IL-4 exhibited low capacities, especially at high rates. This can be attributed to the poor Li^+ conductivity of the $TFSI^-$-derived SEI [40]. Of note, the electrode high-rate performance measured for the conventional $LiPF_6$/EC:DEC electrolyte (in Fig. S2) is also inferior to that found for Pyr_{12O1}FTFSI-2. This is particularly remarkable, since the rate capability of IL-comprising cells is usually low. Our proposed IL electrolyte, however, has great potential to overcome this limitation.

Fig. 4(f) shows the EIS data of various cells acquired after two conditioning cycles. The Nyquist plots show a semicircle at high frequencies and a sloping line at low frequencies, which can be characterized by the equivalent circuit shown in the inset of Fig. 4(f), where R_e, R_{ct}, *CPE*, and *W* represent the electrolyte resistance, charge transfer resistance, interfacial constant phase element, and Warburg impedance associated with Li^+ diffusion within the electrode, respectively [41]. The fitting results indicate that the R_{ct} values, which correspond to the diameters of the semicircles, are 48, 30, 35, and 115 Ω for the Pyr_{12O1}FTFSI-1, Pyr_{12O1}FTFSI-2, IL-3, and IL-4 cells, respectively. The R_{ct} trend is in line with the electrode high-rate properties presented in Fig. 4(e).

To gain more insight into the SEI chemistry, XPS was applied to the Si/CNT/G electrodes, which were subjected to three charge–discharge cycles at 50 mA g^{-1} in various electrolytes. Fig. 5(a) shows the C 1s spectra of the samples, which can be split into several constituents. In addition to the main C–C bonding peak at 284.6 eV, additional peaks for C—O (286.5 eV), O—C═O (288.5 eV), and CO_3^{2-} (289.9 eV) were observed [42,43]. The ether group in the side chain of Pyr_{12O1} promotes the formation of oxygen-containing species in the SEI. An excessive amount of organic species hindered Li^+ ion transport and the desolvation reaction of Li^+ [44,45], contributing to the inferior performance of the Pyr_{12O1}FTFSI-1 cell (vs. Pyr_{12O1}FTFSI-2 and IL-3 cells). There is an additional signal at ~292.5 eV for both FTFSI- and TFSI-based electrolytes, which can be ascribed to the C–F bond (from TFSI moieties). For the IL-4 sample, the SEI chemistry is quite distinct (i.e., absence of O—C═O and CO_3^{2-} species). This explains the entirely

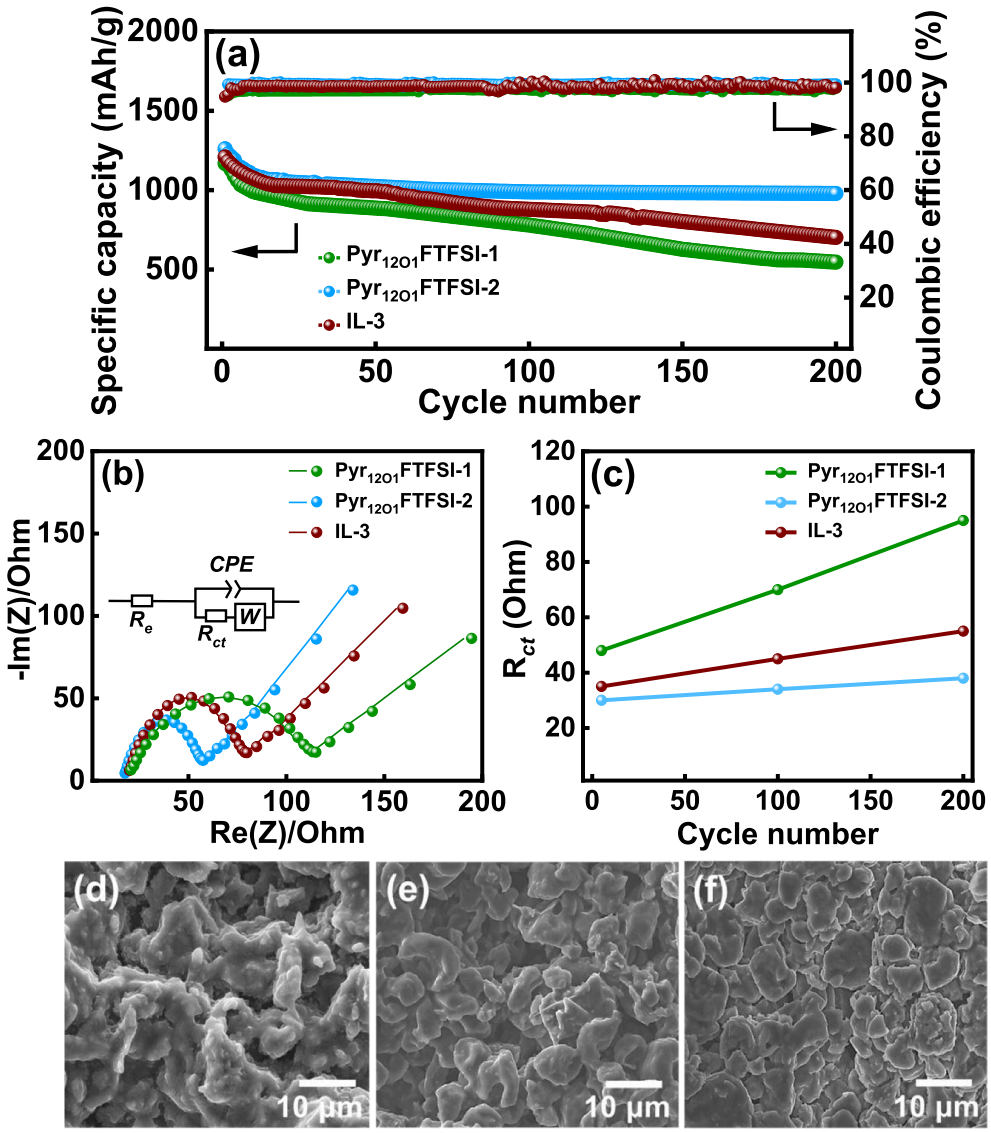

Fig. 6. (a) Cycling stability, (b) EIS spectra after 200 charge–discharge cycles (solid spheres represent data points and solid lines represent fitting curves), and (c) variations of R_{ct} with the cycle number of Si/CNT/G electrodes measured in various electrolytes. SEM images of Si/G/CNT electrodes after cycling in (d) $Pyr_{12O1}FTFSI$-1, (e) $Pyr_{12O1}FTFSI$-2, and (f) IL-3 electrolytes for 200 times.

different electrochemical behavior of this electrode from that of the other electrodes (Fig. 4). The F 1s spectra (Fig. 5(b)) consist of two peaks, which are related to LiF and incomplete IL anion decomposition (S—F/C—F bonding), respectively. As shown, the $Pyr_{12O1}FTFSI$-2 electrode shows the highest LiF fraction. The LiF compound, which is chemically stable and has an insulating nature, can effectively passivate the electrode surface [46]. This contributes to its highest initial CE observed in Fig. S1(b). With a high Li^+ fraction of $Pyr_{12O1}FTFSI$-2, the electrons of $FTFSI^-$ anions are substantially drawn. The less negative $FTFSI^-$ anions thus became more susceptible to reduction, tending to produce LiF. The $TFSI^-$ anions are not easily decomposed; the LiF signal is thus small. For the N 1s spectra (Fig. 5(c)), a peak associated with pyrrolidinium cations (at ~403.3 eV) and a peak associated with imide anions (at ~400 eV) are observed [47]. Besides, a signal corresponding to Li_3N (at ~398 eV) is clearly found for the FTFSI and FSI samples (this signal is small for the TFSI sample). The high Li^+ fraction of $Pyr_{12O1}FTFSI$-2 promotes anion decomposition, resulting in the high Li_3N concentration on the electrode surface. It is worth mentioning that the Li_3N compound both maintains the mechanical robustness of the SEI and provides high Li^+ conductivity [47,48]. Of note, the SEI layer produced from $Pyr_{12O1}FTFSI$-2 IL has high amounts of both protective LiF and conductive Li_3N. This unique composition of the SEI is responsible for the superior CE and rate capability of the Si/CNT/G electrode.

Fig. 6(a) compares the cycling stability data of the Si/CNT/G electrodes measured in various IL electrolytes at a specific current of 100 mA g^{-1}. After 200 charge–discharge cycles, the capacity retention ratios for the $Pyr_{12O1}FTFSI$-1, $Pyr_{12O1}FTFSI$-2, and IL-3 cells were 50%, 80%, and 60%, respectively. The IL-4 cell was not further evaluated due to its poor charge–discharge performance. Fig. 6(b) shows the EIS spectra of the electrodes after cycling. As illustrated in Fig. 6(c), the R_{ct} values of the three cells reached 95 Ω (98% increase), 38 Ω (27% increase), and 55 Ω (57% increase), respectively, after 200 cycles. The relatively small R_{ct} increase of the $Pyr_{12O1}FTFSI$-2 cell can be attributed to the robust LiF- and Li_3N-rich SEI. Fig. 6 (d) (f) show the postmortem SEM images of the Si/CNT/G electrodes after cycling. Basically, the electrode structures were preserved (compared to the as-fabricated electrode (Fig. S4)). The interweaving CNTs and wrapping graphitic sheets effectively accommodate the volume variation of Si particles, leading to the decent integrity of the electrodes. However, we did observe distinct surface morphologies of the electrodes cycled in various electrolytes.

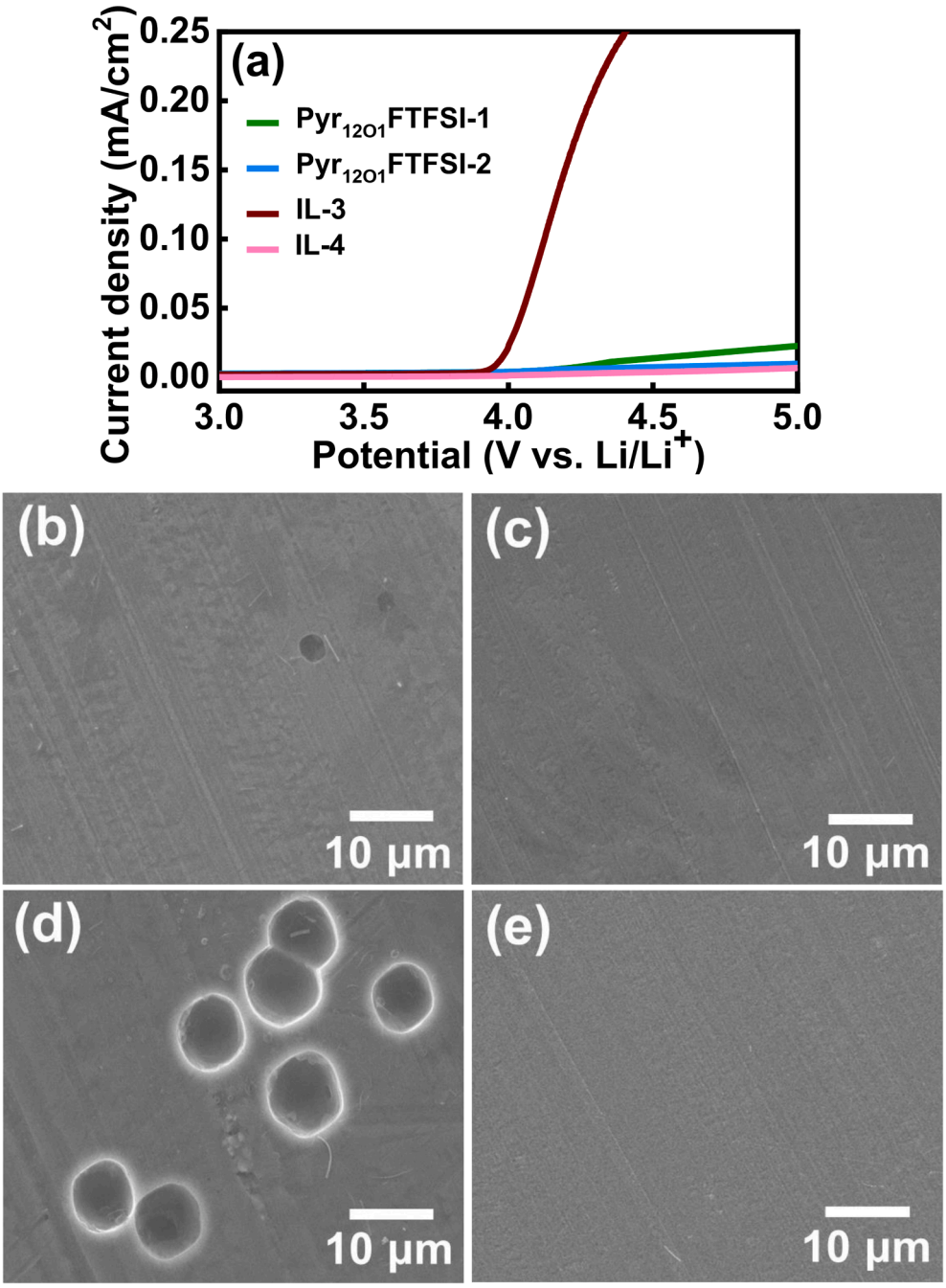

Fig. 7. (a) LSV curves of Al electrodes recorded in various electrolytes with potential scan rate of 1 mV s ^{1}. SEM images of Al electrodes subjected to 5-V polarization for 12 h in (b) $Pyr_{12O1}FTFSI$-1, (c) $Pyr_{12O1}FTFSI$-2, (d) IL-3, and (e) IL-4 electrolytes.

$Pyr_{12O1}FTFSI$-1 produced a thick and nonuniform SEI layer because the organic-species-rich SEI did not effectively passivate the electrode [49]. The relatively low CE reflects the continuous decomposition of the electrolyte. The excessive formation of the SEI hindered Li^+ transport and resulted in noticeable capacity fading. In contrast, the SEI generated in IL-3 was dominated by inorganic components (i.e., high LiF, but low C–O/O–C O content), which can be brittle and poorly adhered [50,51]. It is easily broken down and reformed during cycling, leading to SEI accumulation. $Pyr_{12O1}FTFSI$-2 produced an organic–inorganic well-balanced SEI that most effectively stabilized the electrode/electrolyte interface. Organic species at a proper amount can act as binders and strain buffers in the SEI, increasing mechanical toughness [50,52], and the LiF and Li_3N compounds provide high passivation ability [53,54]. Therefore, the electrode structure is retained to the highest extent, explaining the superior cycling stability of the cell comprising $Pyr_{12O1}FTFSI$-2. It was reported that an advanced binder can minimize mechanical degradation and thus further improve durability of a Si-based electrode [15]. This strategy could be incorporated to increase the electrode cyclability in the $Pyr_{12O1}FTFSI$-2 electrolyte.

Electrolyte compatibility toward the positive electrode is important for practical LIB implementations. Fig. 7(a) shows the linear sweep voltammetry (LSV) curves of Al electrodes measured in various electrolytes. The Al electrodes subjected to 5-V polarization for 12 h were examined using SEM. The data obtained are shown in Fig. 7(b) (e). An SEM image of the pristine Al electrode is provided in Fig. S5 for comparison. In IL-3, a strong irreversible oxidation current emerged before 4 V. The SEM image confirms that this anodic reaction is related to Al pitting corrosion. FSI^- anions are prone to react with Al, forming soluble

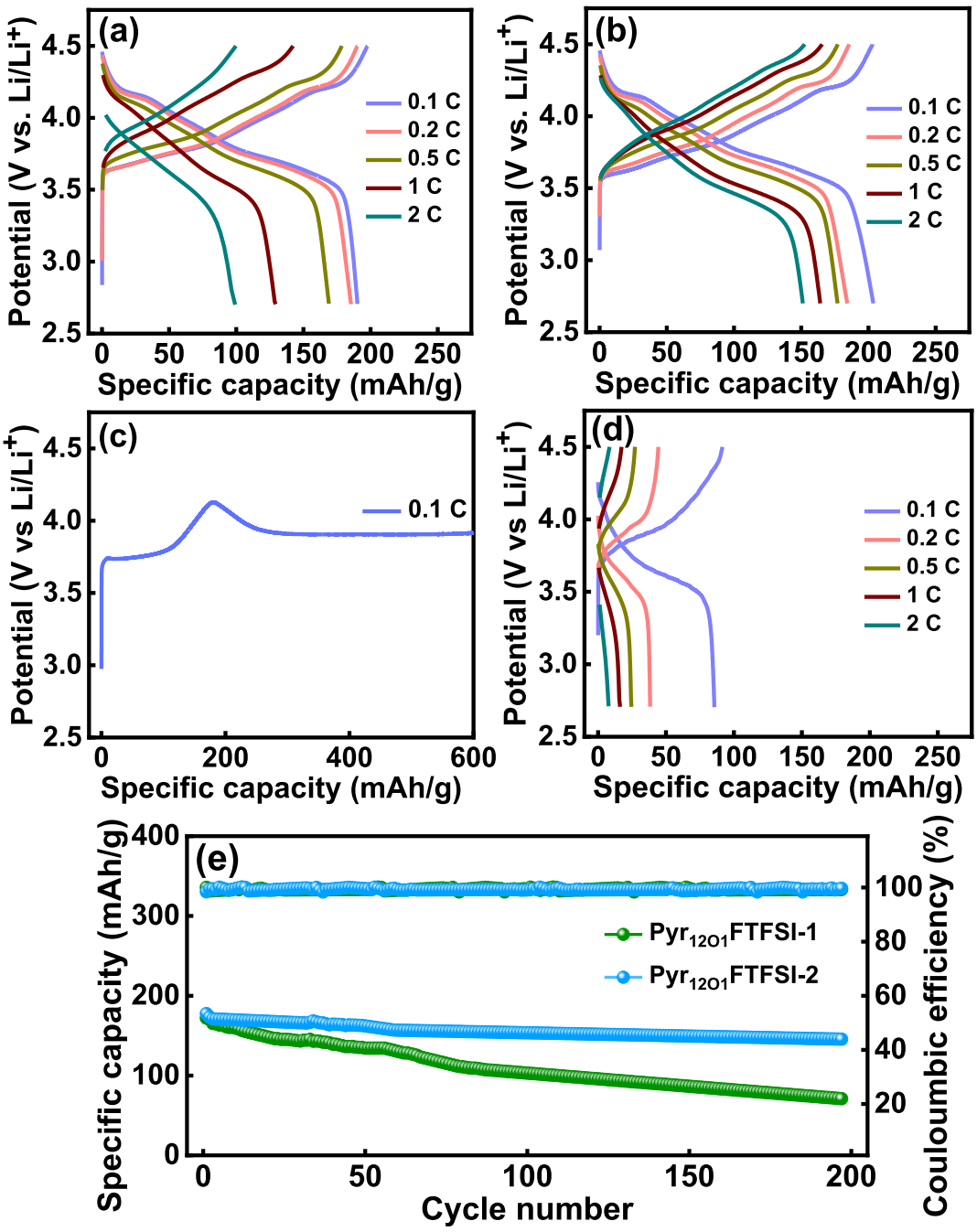

Fig. 8. Charge discharge curves of NCM-811 electrodes recorded in (a) $Pyr_{12O1}FTFSI$-1, (b) $Pyr_{12O1}FTFSI$-2, (c) IL-3, and (d) IL-4 electrolytes at various current rates. (e) Cycling stability of NCM-811 electrodes measured in $Pyr_{12O1}FTFSI$-1 and $Pyr_{12O1}FTFSI$-2 electrolytes.

Table 2
Reversible capacities (mAh g^{-1}) of NCM-811 electrodes measured at various rates in IL electrolytes.

Specific current (C)	$Pyr_{12O1}FTFSI$-1	$Pyr_{12O1}FTFSI$-2	IL-3	IL-4
0.1	190	204	–	86
0.2	185	186	–	39
0.5	169	177	–	25
1	129	164	–	16
2	99	155	–	8
$\frac{\text{Capacity@2 C}}{\text{Capacity@0.1 C}}$(%)	52	76	–	9

Al–FSI complexes [55]. This problem hinders FSI-based IL electrolytes for high-voltage LIB applications. As shown in Fig. S6, even when the LiFSI to $Pyr_{13}FSI$ molar ratio was increased to 3:7, serious Al dissolution still occurred. In contrast, it is found that the Al corrosion in FTFSI-based IL electrolytes was significantly suppressed, indicating a lower complexing ability of $FTFSI^-$ (vs. FSI^-) toward Al. As shown in Fig. 7(a), the high Li^+ fraction of $Pyr_{12O1}FTFSI$-2 can further reduce Al corrosion. The high Li^+ concentration promotes the formation of $Li^+/FTFSI^-$ contact ion pairs and ion aggregates [56,57]. Because there are fewer free $FTFSI^-$ anions to coordinate Al, the LSV oxidation current decreases. Although IL-4 had poor performance in terms of forming an effective SEI, it showed a wide electrochemical stability window and little Al corrosion [58,59]. According to the LSV and SEM data in Fig. 7, the Al corrosivity of $Pyr_{12O1}FTFSI$-2 is as low as that of IL-4.

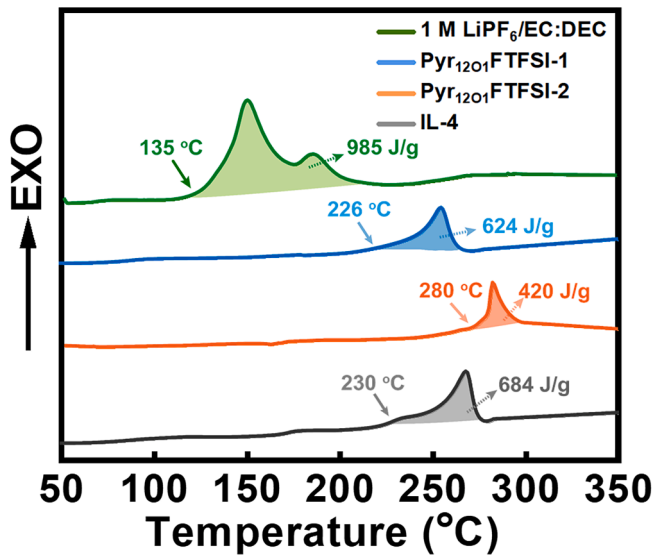

Fig. 9. DSC data of delithiated NCM-811 samples with various electrolytes.

Fig. 8(a) (d) show the charge–discharge curves of the NCM-811 half cells with Pyr_{1201}FTFSI-1, Pyr_{1201}FTFSI-2, IL-3, and IL-4 electrolytes, respectively, within a voltage range of 2.7–4.5 V (vs. Li^+/Li). With the IL-3 electrolyte, the charging voltage did not reach the cut-off value and leveled off at ~4 V. This can be ascribed to the occurrence of Al dissolution side reactions, which consume the applied current. Although this IL works well with the Si/CNT/G anode, its cathode compatibility is poor. As shown, the IL-4 cell exhibits low charge–discharge capacities, probably due to the highly resistive SEI on the Li anode surface. The measured capacities of NCM-811 at 0.1C with Pyr_{1201}FTFSI-1 and Pyr_{1201}FTFSI-2 electrolytes were 190 and 204 mAh g^{-1}, respectively (1C 275 mA g^{-1}). At 2C, the reversible capacities decreased to 99 and 151 mAh g^{-1}, respectively, corresponding to 52% and 74% retention compared to the values obtained at 0.1C (Table 2). Fig. 8(e) compares the cycling stability data of the NCM-811 half cells with various electrolytes recorded at 0.5C. The capacity retention ratios of the Pyr_{1201}FTFSI-1 and Pyr_{1201}FTFSI-2 cells after 200 charge–discharge cycles are 37% and 85%, respectively. The superior rate capability and cyclability found for the latter cell can be attributed to the suppressed Al current collector corrosion. Moreover, as shown in Fig. S7, the NCM-811 surface morphology and EIS impedance remain stable upon cycling in the Pyr_{1201}FTFSI-2 electrolyte. As shown in Fig. S8, the conventional 1 M $LiPF_6$/EC:DEC electrolyte NCM-811 half cell retained only 8% of its initial capacity after the same number of charge–discharge cycles. At the high-Ni-content NCM-811 surface, carbonate electrolyte decomposition and interfacial side reactions are promoted at high potential [60], leading to rapid cell deterioration. The proposed high-Li^+-fraction Pyr_{1201}FTFSI-2 IL electrolyte is highly promising for high-voltage Ni-rich NCM cells.

To assess the safety properties, the interfacial exothermic reactions between the delithiated NCM-811 and various electrolytes were examined using DSC. As shown in Fig. 9, the sample with the conventional 1 M $LiPF_6$/EC:DEC electrolyte exhibits an exothermic onset at ~135 °C, which is attributed to the electrolyte decomposition catalyzed by the fully charged (thus highly active) NCM-811 surface and the phase degradation (to spinel/rock-salt phases) of the layer-structure NCM-811 [61,62]. The shoulder at a higher temperature can be ascribed to the breaking of metal–oxygen bonds and thus oxygen release from the NCM-811 lattice [63,64]. The overall heat released is as high as 985 J g^{-1}, indicating a vigorous interfacial exothermic reaction. In contrast, the samples with IL electrolytes showed considerably higher exothermic onset temperatures and less heat generation, as depicted in Fig. 9. This confirms the high safety of using IL electrolytes in LIBs. Among them, the Pyr_{1201}FTFSI-2 sample exhibited the best thermal stability, with an onset temperature of 280 °C and a total heat of 420 J g^{-1}. The high LiFTFSI content of this IL reduced the organic pyrrolidinium cation fraction, increasing electrolyte thermal stability [65]. The experimental results also suggest that Pyr_{1201}FTFSI-2 produced a cathode/electrolyte interphase that can better stabilize the delithiated NCM-811, mitigating the structural deterioration and metal–oxygen bond breaking reactions.

The Si/CNT/G||NCM-811 full cells were assembled, as depicted in Fig. 10(a), to evaluate the effects of electrolyte composition on the overall battery performance. Fig. 10(b)–(d) compare the charge–discharge profiles of the full cells containing the conventional 1 M $LiPF_6$/EC:DEC, Pyr_{1201}FTFSI-1, and Pyr_{1201}FTFSI-2 electrolytes, respectively. The last cell clearly outperformed the others in terms of maximum capacity and rate capability. These results are consistent with the half-cell testing results. Fig. 10(e) shows the cycling stability data of the three full cells evaluated at a rate of 0.5C. The 1 M $LiPF_6$/EC:DEC and Pyr_{1201}FTFSI-1 cells died (capacity faded to zero) after 70 and 100 cycles, respectively. The Pyr_{1201}FTFSI-2 cell exhibited the best cyclability. After 300 cycles, its capacity retention was 80%, with a charge–discharge CE of ~99.9%. This can be attributed to the superior compatibility of the proposed electrolyte toward both the high-capacity Si/CNT/G anode and the Ni-rich high-voltage NCM-811 cathode.

4. Conclusions

A unique combination of Pyr_{1201}^+ and $FTFSI^-$ enables a high fraction of Li^+ in an IL electrolyte. This electrolyte was for the first time adopted for Si/CNT/G||NCM-811 LIBs. The ether side chain on Pyr_{1201} creates organic C—O/O—C═O species in the SEI. The high Li^+ fraction promotes $FTFSI^-$ decomposition, producing a LiF- and Li_3N-rich SEI. The unique SEI composition makes the rate capability of Si/CNT/G in the Pyr_{1201}FTFSI-2 electrolyte higher than that in the conventional 1 M $LiPF_6$/EC:DEC electrolyte. With this SEI, the electrode cycling stability in this electrolyte outperforms that found for the FSI-based IL electrolyte, which is known to favor Si anode durability. $FTFSI^-$ anions show low corrosivity toward Al. An increase in Li^+ concentration in the IL electrolyte can further suppress the Al corrosion current. The Pyr_{1201}FTFSI-2 electrolyte shows high compatibility with the Ni-rich NCM-811 cathode up to 4.5 V. A remarkable capacity of >200 mAh g^{-1} and a superior cycle life were achieved for NCM-811. The DSC data indicate that the Pyr_{1201}FTFSI-2 electrolyte can effectively suppress the interfacial exothermic reactions of delithiated NCM-811, thus increasing battery safety. The Si/CNT/G||NCM-811 full cell with the Pyr_{1201}FTFSI-2 electrolyte has better high-rate performance (150 mAh g^{-1}@2C based on NCM-811) and cyclability (80% retention after 300 cycles) than those of cells with the low-Li^+-fraction Pyr_{1201}FTFSI-1 and conventional carbonate electrolytes. The proposed electrolyte composition and design strategies have great potential for use in high-energy-density and high-reliability LIBs.

Declaration of Competing Interest

The authors declare that they have no known competing financial interests or personal relationships that could have appeared to influence the work reported in this paper.

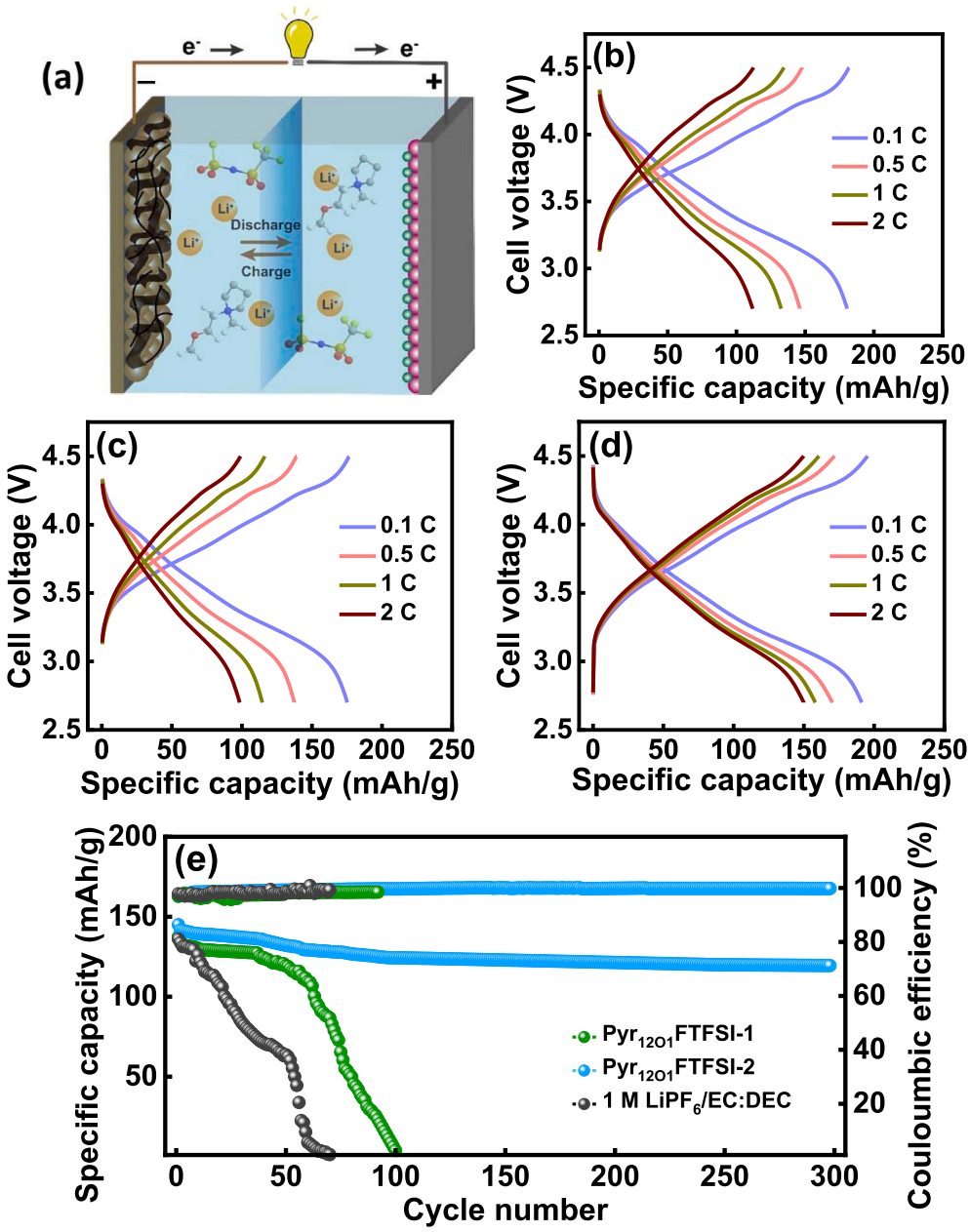

Fig. 10. (a) Scheme of LIB full cell using Si/CNT/G anode and NCM-811 cathode. Charge–discharge curves of Si/CNT/G||NCM-811 full cells with (b) 1 M $LiPF_6$/EC:DEC, (c) Pyr_{12O1}FTFSI-1, and (d) Pyr_{12O1}FTFSI-2 electrolytes. (e) Cycling stability of Si/CNT/G||NCM-811 full cells with various electrolytes.

Acknowledgments

The financial support provided for this work by the Ministry of Science and Technology (MOST) of Taiwan is gratefully appreciated. X.G., D.B., and S.P. acknowledge funding from the Helmholtz Association and the German Federal Ministry of Education and Research (BMBF) within the High-Safe (03XP0138C) and HighSafe-II (03XP0306C) projects.

Appendix A. Supplementary data

Supplementary data to this article can be found online at https://doi.org/10.1016/j.cej.2021.132693.

References

[1] E. Fan, L.i. Li, Z. Wang, J. Lin, Y. Huang, Y. Yao, R. Chen, F. Wu, Sustainable recycling technology for Li-ion batteries and beyond: Challenges and future prospects, Chem. Rev. 120 (14) (2020) 7020–7063, https://doi.org/10.1021/acs.chemrev.9b00535.

[2] F. Wu, J. Maier, Y. Yu, Guidelines and trends for next-generation rechargeable lithium and lithium-ion batteries, Chem. Soc. Rev. 49 (5) (2020) 1569–1614, https://doi.org/10.1039/C7CS00863E.

[3] T. Kim, W. Song, D.-Y. Son, L.K. Ono, Y. Qi, Lithium-ion batteries: Outlook on present, future, and hybridized technologies, J. Mater. Chem. A 7 (7) (2019) 2942–2964, https://doi.org/10.1039/C8TA10513H.

[4] T.X. Nguyen, J. Patra, J.-K. Chang, J.-M. Ting, High entropy spinel oxide nanoparticles for superior lithiation–delithiation performance, J. Mater. Chem. A 8 (36) (2020) 18963–18973, https://doi.org/10.1039/D0TA04844E.

[5] H.-Y. Li, C.-M. Tseng, C.-H. Yang, T.-C. Lee, C.-Y. Su, C.-T. Hsieh, J.-K. Chang, Eco-efficient synthesis of highly porous $CoCO_3$ anodes from supercritical CO_2 for Li^+ and Na^+ storage, ChemSusChem 10 (11) (2017) 2464–2472, https://doi.org/10.1002/cssc.201700171.

[6] J. Asenbauer, T. Eisenmann, M. Kuenzel, A. Kazzazi, Z. Chen, D. Bresser, The success story of graphite as a lithium-ion anode material–fundamentals, remaining challenges, and recent developments including silicon (oxide) composites, Sustainable Energy Fuels 4 (11) (2020) 5387–5416, https://doi.org/10.1039/D0SE00175A.

[7] H. Wu, Y.i. Cui, Designing nanostructured Si anodes for high energy lithium ion batteries, Nano Today 7 (5) (2012) 414–429, https://doi.org/10.1016/j.nantod.2012.08.004.

[8] B. Zhu, X. Wang, P. Yao, J. Li, J. Zhu, Towards high energy density lithium battery anodes: Silicon and lithium, Chem. Sci. 10 (2019) 7132–7148, https://doi.org/10.1039/C9SC01201J.

[9] K. Feng, M. Li, W. Liu, A.G. Kashkooli, X. Xiao, M. Cai, Z. Chen, Silicon-based anodes for lithium-ion batteries: From fundamentals to practical applications, Small 14 (8) (2018) 1702737, https://doi.org/10.1002/smll.v14.810.1002/smll.201702737.

[10] Y. Jin, B. Zhu, Z. Lu, N. Liu, J. Zhu, Challenges and recent progress in the development of Si anodes for lithium-ion battery, Adv. Energy Mater. 7 (23) (2017) 1700715, https://doi.org/10.1002/aenm.201700715.

[11] T. Song, J. Xia, J.-H. Lee, D.H. Lee, M.-S. Kwon, J.-M. Choi, J. Wu, S.K. Doo, H. Chang, W.I. Park, D.S. Zang, H. Kim, Y. Huang, K.-C. Hwang, J.A. Rogers, U. Paik, Arrays of sealed silicon nanotubes as anodes for lithium ion batteries, Nano Lett. 10 (5) (2010) 1710–1716, https://doi.org/10.1021/nl100086e.

[12] M. Gu, Y. He, J.M. Zheng, C.M. Wang, Nanoscale silicon as anode for Li-ion batteries: The fundamentals, promises, and challenges, Nano Energy 17 (2015) 366–383, https://doi.org/10.1016/j.nanoen.2015.08.025.

[13] H. Wu, G. Chan, J.W. Choi, I. Ryu, Y. Yao, M.T. McDowell, S.W. Lee, A. Jackson, Y. Yang, L. Hu, Y.i. Cui, Stable cycling of double-walled silicon nanotube battery anodes through solid–electrolyte interphase control, Nat. Nanotechnol. 7 (5) (2012) 310–315, https://doi.org/10.1038/nnano.2012.35.

[14] F. Luo, B.N. Liu, J.Y. Zheng, G. Chu, K.F. Zhong, H. Li, X.J. Huang, L.Q. Chen, Nano-silicon/carbon composite anode materials towards practical application for next generation Li-ion batteries, J. Electrochem. Soc. 162 (2015) A2509–A2528, https://doi.org/10.1149/2.0131514jes.

[15] T.-W. Kwon, J.W. Choi, A. Coskun, The emerging era of supramolecular polymeric binders in silicon anodes, Chem. Soc. Rev. 47 (6) (2018) 2145–2164, https://doi.org/10.1039/C7CS00858A.

[16] J. Chen, X. Fan, Q. Li, H. Yang, M.R. Khoshi, Y. Xu, S. Hwang, L. Chen, X. Ji, C. Yang, H. He, C. Wang, E. Garfunkel, D. Su, O. Borodin, C. Wang, Electrolyte design for LiF-rich solid–electrolyte interfaces to enable high-performance microsized alloy anodes for batteries, Nat. Energy 5 (5) (2020) 386–397, https://doi.org/10.1038/s41560-020-0601-1.

[17] K. Arano, S. Begic, F. Chen, D. Rakov, D. Mazouzi, N. Gautier, R. Kerr, B. Lestriez, J. Le Bideau, P.C. Howlett, D. Guyomard, M. Forsyth, N. Dupre, Tuning the formation and structure of the silicon electrode/ionic liquid electrolyte interphase in superconcentrated ionic liquids, ACS Appl. Mater. Interfaces 13 (24) (2021) 28281–28294, https://doi.org/10.1021/acsami.1c06465.

[18] M. Watanabe, M.L. Thomas, S. Zhang, K. Ueno, T. Yasuda, K. Dokko, Application of ionic liquids to energy storage and conversion materials and devices, Chem. Rev. 117 (10) (2017) 7190–7239, https://doi.org/10.1021/acs.chemrev.6b00504.

[19] A. Eftekhari, Y. Liu, P. Chen, Different roles of ionic liquids in lithium batteries, J. Power Sources 334 (2016) 221–239, https://doi.org/10.1016/j.jpowsour.2016.10.025.

[20] J. Patra, P.P. Dahiya, C.J. Tseng, J. Fang, Y.W. Lin, S. Basu, S. Majumder, J. K. Chang, Electrochemical performance of 0.5 Li_2MnO_3–0.5 Li($Mn_{0.375}Ni_{0.375}Co_{0.25}$) O_2 composite cathode in pyrrolidinium-based ionic liquid electrolytes, J. Power Sources 294 (2015) 22–30, https://doi.org/10.1016/j.jpowsour.2015.06.035.

[21] P.C. Rath, C.-J. Wu, J. Patra, J. Li, T.-C. Lee, T.-J. Yeh, J.K. Chang, Hybrid electrolyte enables safe and practical 5 V $LiNi_{0.5}Mn_{1.5}O_4$ batteries, J. Mater. Chem. A 7 (27) (2019) 16516–16525, https://doi.org/10.1039/C9TA04147H.

[22] J. Hu, Z. Yao, K. Chen, C. Li, High-conductivity open framework fluorinated electrolyte bonded by solidified ionic liquid wires for solid-state Li metal batteries, Energy Storage Mater. 28 (2020) 37–46, https://doi.org/10.1016/j.ensm.2020.02.018.

[23] J. Hu, K. Chen, C. Li, Nanostructured Li-rich fluoride coated by ionic liquid as high ion-conductivity solid electrolyte additive to suppress dendrite growth at Li metal anode, ACS Appl. Mater. Interfaces 10 (40) (2018) 34322–34331, https://doi.org/10.1021/acsami.8b12579.

[24] N.S. Ramirez, B.D. Assresahegn, R.M. Torresi, D. Belanger, Producing high-performing silicon anodes by tailoring ionic liquids as electrolytes, Energy Storage Mater. 25 (2020) 477–486, https://doi.org/10.1016/j.ensm.2019.09.035.

[25] Y. Domi, H. Usui, K. Yamaguchi, S. Yodoya, H. Sakaguchi, Silicon-based anodes with long cycle life for lithium-ion batteries achieved by significant suppression of their volume expansion in ionic-liquid electrolyte, ACS Appl. Mater. Interfaces 11 (3) (2019) 2950–2960, https://doi.org/10.1021/acsami.8b17123.

[26] D.M. Piper, T. Evans, K. Leung, T. Watkins, J. Olson, S.C. Kim, S.S. Han, V. Bhat, K. H. Oh, D.A. Buttry, S.H. Lee, Stable silicon-ionic liquid interface for next-generation lithium-ion batteries, Nat. Commun. 6 (2015) 6230, https://doi.org/10.1038/ncomms7230.

[27] P.C. Rath, Y.-W. Wang, J. Patra, B. Umesh, T.-J. Yeh, S. Okada, J. Li, J.-K. Chang, Composition manipulation of bis(fluorosulfonyl)imide-based ionic liquid electrolyte for high-voltage graphite//$LiNi_{0.5}Mn_{1.5}O_4$ lithium-ion batteries, Chem. Eng. J. 415 (2021) 128904, https://doi.org/10.1016/j.cej.2021.128904.

[28] S. Theivaprakasam, G. Girard, P. Howlett, M. Forsyth, S. Mitra, D. MacFarlane, Passivation behaviour of aluminium current collector in ionic liquid alkyl carbonate (hybrid) electrolytes, NPJ Mater. Degrad. 2 (2018) 13, https://doi.org/10.1038/s41529-018-0033-6.

[29] X. Gao, F. Wu, A. Mariani, S. Passerini, Concentrated ionic-liquid-based electrolytes for high-voltage lithium batteries with improved performance at room temperature, ChemSusChem 12 (2019) 4185–4193, https://doi.org/10.1002/cssc.201901739.

[30] J. Reiter, S. Jeremias, E. Paillard, M. Winter, S. Passerini, Fluorosulfonyl-(trifluoromethanesulfonyl) imide ionic liquids with enhanced asymmetry, Phys. Chem. Chem. Phys. 15 (2013) 2565–2571, https://doi.org/10.1039/C2CP43066E.

[31] W. Tu, G. Szklarz, K. Adrjanowicz, K. Grzybowska, J. Knapik-Kowalczuk, M. Paluch, Effect of cation n-Alkyl side-chain length, temperature, and pressure on the glass-transition dynamics and crystallization tendency of the $[C_nC_1Pyrr]^+[Tf_2N]$ ionic liquid family, J. Phys. Chem. C 123 (20) (2019) 12623–12637, https://doi.org/10.1021/acs.jpcc.9b0268910.1021/acs.jpcc.9b02689.s001.

[32] M. Kunze, E. Paillard, S. Jeong, G.B. Appetecchi, M. Schonhoff, M. Winter, S. Passerini, Inhibition of self-aggregation in ionic liquid electrolytes for high-energy electrochemical devices, J. Phys. Chem. C 115 (39) (2011) 19431–19436, https://doi.org/10.1021/jp2055969.

[33] G.A. Giffin, Ionic liquid-based electrolytes for "beyond lithium" battery technologies, J. Mater. Chem. A 4 (35) (2016) 13378–13389, https://doi.org/10.1039/C6TA05260F.

[34] T. Li, X.-Z. Yuan, L. Zhang, D. Song, K. Shi, C. Bock, Degradation mechanisms and mitigation strategies of nickel-rich NMC-based lithium-ion batteries, Electrochem. Energ. Rev. 3 (1) (2020) 43–80, https://doi.org/10.1007/s41918-019-00053-3.

[35] G.B. Appetecchi, S. Scaccia, C. Tizzani, F. Alessandrini, S. Passerini, Synthesis of hydrophobic ionic liquids for electrochemical applications, J. Electrochem. Soc. 153 (2006) A1685–A1691, https://doi.org/10.1149/1.2213420.

[36] S. Schipporeit, D. Mergel, Spectral decomposition of Raman spectra of mixed-phase TiO_2 thin films on Si and silicate substrates, J. Raman Spectrosc. 49 (2018) 1217–1229, https://doi.org/10.1002/jrs.5369.

[37] A. Jorio, M.S. Dresselhaus, R. Saito, G. Dresselhaus, Raman spectroscopy in graphene related systems, John Wiley & Sons, 2011.

[38] E. Peled, S. Menkin, SEI: Past, present and future, J. Electrochem. Soc. 164 (2017) A1703–A1719, https://doi.org/10.1149/2.1441707jes.

[39] G.A. Giffin, A. Moretti, S. Jeong, K. Pilar, M. Brinkkotter, S.G. Greenbaum, M. Schonhoff, S. Passerini, Connection between lithium coordination and lithium diffusion in [Pyr_{12O1}] [FTFSI] ionic liquid electrolytes, ChemSusChem 11 (12) (2018) 1981–1989, https://doi.org/10.1002/cssc.201702288.

[40] N. Nakatani, K. Kishida, K. Nakagawa, Effect of SEI component on graphite electrode performance for Li-ion battery using ionic liquid electrolyte, J. Electrochem. Soc. 165 (9) (2018) A1621–A1625, https://doi.org/10.1149/2.0361809jes.

[41] C.-J. Wu, P.C. Rath, J. Patra, D. Bresser, S. Passerini, B. Umesh, Q.-F. Dong, T.-C. Lee, J.-K. Chang, Composition modulation of ionic liquid hybrid electrolyte for 5 V lithium-ion batteries, ACS Appl. Mater. Interfaces 11 (45) (2019) 42049–42056, https://doi.org/10.1021/acsami.9b12915.

[42] B. Philippe, R. Dedryvère, M. Gorgoi, H. Rensmo, D. Gonbeau, K. Edstrom, Improved performances of nano silicon electrodes using the salt LiFSI: A photoelectron spectroscopy study, J. Am. Chem. Soc. 135 (26) (2013) 9829–9842, https://doi.org/10.1021/ja403082s.

[43] B. Umesh, P.C. Rath, R.F.H. Hernandha, J.-Y. Lin, S.B. Majumder, Q.-F. Dong, J.-K. Chang, Moderate-concentration fluorinated electrolyte for high-energy-density Si//$LiNi_{0.8}Co_{0.1}Mn_{0.1}O_2$ batteries, ACS Sustain, Chem. Eng. 8 (43) (2020) 16252–16261, https://doi.org/10.1021/acssuschemeng.0c05560.

[44] J.-D. Xie, J. Patra, P.C. Rath, W.-J. Liu, C.-Y. Su, S.-W. Lee, C.-J. Tseng, Y. A. Gandomi, J.-K. Chang, Highly concentrated carbonate electrolyte for Li-ion batteries with lithium metal and graphite anodes, J. Power Sources 450 (2020) 227657, https://doi.org/10.1016/j.jpowsour.2019.227657.

[45] K. Xu, A. Cresce, U. Lee, Differentiating contributions to "ion transfer" barrier from interphasial resistance and Li^+ desolvation at electrolyte/graphite interface, Langmuir 26 (13) (2010) 11538–11543, https://doi.org/10.1021/la1009994.

[46] J. Lin, H.u. Peng, J.-H. Kim, B.R. Wygant, M.L. Meyerson, R. Rodriguez, Y. Liu, K. Kawashima, D. Gu, D.-L. Peng, H. Guo, A. Heller, C.B. Mullins, Lithium fluoride coated silicon nano columns as anodes for lithium ion batteries, ACS Appl. Mater. Interfaces 12 (16) (2020) 18465–18472, https://doi.org/10.1021/acsami.9b23106.

[47] I. Weber, J. Kim, F. Buchner, J. Schnaidt, R.J. Behm, Surface science and electrochemical model studies on the interaction of graphite and Li-containing ionic liquids, ChemSusChem 13 (10) (2020) 2589–2601, https://doi.org/10.1002/cssc.v13.1010.1002/cssc.202000495.

[48] K. Chen, R. Pathak, A. Gurung, E.A. Adhamash, B. Bahrami, Q. He, H. Qiao, A. L. Smirnova, J.J. Wu, Q. Qiao, Y. Zhou, Flower-shaped lithium nitride as a protective layer via facile plasma activation for stable lithium metal anodes, Energy Storage Mater. 18 (2019) 389–396, https://doi.org/10.1016/j.ensm.2019.02.006.

[49] W. Huang, P.M. Attia, H. Wang, S.E. Renfrew, N. Jin, S. Das, Z. Zhang, D.T. Boyle, Y. Li, M.Z. Bazant, B.D. McCloskey, W.C. Chueh, Y. Cui, Evolution of the solid–electrolyte interphase on carbonaceous anodes visualized by atomic-resolution cryogenic electron microscopy, Nano Lett. 19 (8) (2019) 5140–5148, https://doi.org/10.1021/acs.nanolett.9b01515.

[50] Q. Shi, S. Heng, Q. Qu, T. Gao, W. Liu, L. Hang, H. Zheng, Constructing an elastic solid electrolyte interphase on graphite: A novel strategy suppressing lithium inventory loss in lithium-ion batteries, J. Mater. Chem. A 5 (22) (2017) 10885–10894, https://doi.org/10.1039/C7TA02706K.

[51] S. Gao, F. Sun, N. Liu, H. Yang, P.F. Cao, Ionic conductive polymers as artificial solid electrolyte interphase films in Li metal batteries–A review, Mater. Today 40 (2020) 140–159, https://doi.org/10.1016/j.mattod.2020.06.011.

[52] S. Ahamad, A. Gupta, Understanding composition and morphology of solid-electrolyte interphase in mesocarbon microbeads electrodes with nano-conducting additives, Electrochim. Acta 341 (2020) 136015, https://doi.org/10.1016/j.electacta.2020.136015

[53] H.-H. Sun, A. Dolocan, J.A. Weeks, R. Rodriguez, A. Heller, C.B. Mullins, In situ formation of a multicomponent inorganic-rich SEI layer provides a fast charging and high specific energy Li-metal battery, J. Mater. Chem. A 7 (30) (2019) 17782–17789, https://doi.org/10.1039/C9TA05063A.
[54] K. Hosoya, T. Kamidaira, T. Tsuda, A. Imanishi, M. Haruta, T. Doi, M. Inaba, S. Kuwabata, Lithium-ion battery performance enhanced by the combination of Si thin flake anodes and binary ionic liquid systems, Mater. Adv. 1 (2020) 625–631, https://doi.org/10.1039/D0MA00296H.
[55] R.S. Kühnel, M. Lübke, M. Winter, S. Passerini, A. Balducci, Suppression of aluminum current collector corrosion in ionic liquid containing electrolytes, J. Power Sources 214 (2012) 178–184, https://doi.org/10.1016/j.jpowsour.2012.04.054.
[56] S.R.G. Kankanamge, D.G. Kuroda, Molecular structure, chemical exchange, and conductivity mechanism of high concentration LiTFSI electrolytes, J. Phys. Chem. B 124 (10) (2020) 1965–1977, https://doi.org/10.1021/acs.jpcb.9b10795.
[57] K. Sodeyama, Y. Yamada, K. Aikawa, A. Yamada, Y. Tateyama, Sacrificial anion reduction mechanism for electrochemical stability improvement in highly concentrated Li-salt electrolyte, J. Phys. Chem. C 118 (26) (2014) 14091–14097, https://doi.org/10.1021/jp501178n.
[58] C. Peng, L.i. Yang, Z. Zhang, K. Tachibana, Y. Yang, S. Zhao, Investigation of the anodic behavior of Al current collector in room temperature ionic liquid electrolytes, Electrochim. Acta 53 (14) (2008) 4764–4772, https://doi.org/10.1016/j.electacta.2008.01.080.
[59] P. Meister, X. Qi, R. Kloepsch, E. Krämer, B. Streipert, M. Winter, T. Placke, Anodic behavior of the aluminum current collector in imide-based electrolytes: Influence of solvent, operating temperature, and native oxide-layer thickness, ChemSusChem 10 (4) (2017) 804–814, https://doi.org/10.1002/cssc.201601636.
[60] H. Gao, X. Zeng, Y. Hu, V. Tileli, L. Li, Y. Ren, X. Meng, F. Maglia, P. Lamp, S.-J. Kim, K. Amine, Z. Chen, Modifying the surface of a high-voltage lithium-ion cathode, ACS Appl. Energy Mater. 1 (5) (2018) 2254–2260, https://doi.org/10.1021/acsaem.8b0032310.1021/acsaem.8b00323.s001.
[61] C.M. Julien, A. Mauger, NCA, NCM 811, and the route to Ni-richer lithium-ion batteries, Energies 13 (2020) 6363, https://doi.org/10.3390/en13236363.
[62] H.M. Barkholtz, Y. Preger, S. Ivanov, J. Langendorf, L. Torres-Castro, J. Lamb, B. Chalamala, S.R. Ferreira, Multi-scale thermal stability study of commercial lithium-ion batteries as a function of cathode chemistry and state-of-charge, J. Power Sources 435 (2019) 226777, https://doi.org/10.1016/j.jpowsour.2019.226777.
[63] F. Mueller, N. Loeffler, G.T. Kim, T. Diemant, R.J. Behm, S. Passerini, A lithium-ion battery with enhanced safety prepared using an environmentally friendly process, ChemSusChem 9 (2016) 1290–1298, https://doi.org/10.1002/cssc201600296.
[64] F. Kong, C. Liang, L. Wang, Y. Zheng, S. Perananthan, R.C. Longo, J.P. Ferraris, M. Kim, K. Cho, Kinetic stability of bulk LiNiO